Available online at www.sciencedirect.com
ScienceDirect
Comput. Methods Appl. Mech. Engrg. 373 (2021) 113486
Computer methods in applied mechanics and engineering
www.elsevier.com/locate/cma

Modeling connected granular media: Particle bonding within the level set discrete element method

John M. Harmon[a], Konstantinos Karapiperis[a], Liuchi Li[a], Scott Moreland[b], José E. Andrade[a,*]

[a] *California Institute of Technology, United States of America*
[b] *Jet Propulsion Laboratory, United States of America*

Received 6 August 2020; received in revised form 23 September 2020; accepted 2 October 2020
Available online 27 November 2020

Abstract

Granular materials are made up of particles with complex non-convex shapes that in many cases become connected by cementation, sintering or other adhesive processes. This paper introduces and describes the methodology behind using the bonded particle method (BPM) with the level set discrete element method (LS-DEM-BPM), in order to model connected granular materials with arbitrary particle shape. The method is thoroughly detailed in both two and three dimensions. Examples of use for the method are shown for three distinct contexts. The first is the modeling of a fault gouge, where it is demonstrated that the method has the potential to be predictive of the rate-and-state friction law and have key insights into the micromechanics of the process. Another example is presented where a cone penetrates porous sintered ice showing that bond thickness has a considerable effect on model behavior. The third example is a simulation using many unique bonds for each contact interface, demonstrating the ability to simulate partial fractures. A discussion is also included on how and when this method can be either advantageous or disadvantageous.

Keywords: Bonding; DEM; Level Set; Fault Rupture; Ice; Granular Materials

1. Introduction

Rocks, ices and metals are among many examples of materials that can be thought of as connected granular materials due to the clear presence of a grain scale that features adhesive mechanisms at grain to grain contact locations. For many applications, the physics at the microscale dominate behavior that is observed at the macroscale. To understand the underlying mechanics of these materials, it is important to model the fundamental physics at the grain scale that drives the macro-scale observations.

For example, considerable study has been done on the microscale of rock and how it affects the macro-scale properties [1,2]. Small flaws in the rock microstructure can cause large differences in fracture strength. This drives the well known phenomenon that as rocks get smaller from breakage their strength increases [3]. The microstructure of ice is also often granular when many ice particles sinter together during formation [4]. The sintering process

* Corresponding author.
E-mail address: jandrade@caltech.edu (J.E. Andrade).

https://doi.org/10.1016/j.cma.2020.113486
0045-7825/

causes the strength of ice to be dependent on the thickness of the sintered neck, which in itself is dependent on time, temperature, humidity and initial particle shapes [5].

The bonded particle method (BPM) has been used in discrete element modeling (DEM) extensively since its introduction by Potyondy & Cundall to model connected granular matter [6]. Particle bonding was originally done with spheres that were bonded by beams connecting the centers of the particles that behave linearly. Progress on the model has usually taken the form of enriching the linear bonding mechanics such as with non-local considerations, or by improving shape capabilities [7,8]. Using spheres assumed that if the spheres were small enough compared to the macro structure that their mechanical response would replicate the granular microstructure of a cemented material. This assumption showed to be effective for simulating aspects of crack propagation in rock [9]. This principle is also used for simulating breakage in sand where every particle is made of many small spheres bonded together during oedometer testing [10,11].

Further developments in both DEM and BPM led to using the bonded particle method in polyheron shaped particles. This was an important development since many studies have shown the importance of particle shape in granular materials [12,13]. The polyhedron based method proved effective for simulating the breakage of rock [14]. This also had important implications for masonry as the shape for bricks could be properly represented [15].

In this paper, the bonded particle model will be implemented with the level set variant of DEM (LS-DEM) for the first time. LS-DEM has key advantages compared to other DEM variants [16]. The most notable is the ability to capture any arbitrary shape for particles without limitations or special treatments. This has allowed the study of granular specimens through a true one-to-one comparison with experiment by utilizing exact shape for every particle from X-ray Computed Tomography (XRCT) imaging [17]. Validation experiments have provided unique levels of confidence in the method which allows for numerical experimentation beyond what is capable in a lab [12,18]. These advantages could often be of interest to applications for the bonded particle model.

This paper is organized as follows. First the model will be described for both two and three dimensions detailing both LS-DEM and bonding where the simple linear version will be used. Three separate examples will be shown each highlighting advantages to using the LS-DEM variant of the bonded particle method. Finally we will conclude with a discussion over both the advantages and disadvantages with the model.

2. Modeling methodology

2.1. Level set discrete element method

LS-DEM is a discrete element modeling variant that utilizes discrete level sets and a surface point discretization for representing particle shape through a leader–follower relationship. Level set functions were developed to define object surfaces implicitly [19]. Discrete level set functions, ϕ, determine the distance, δ, to an object surface given a location, $\mathbf{x}$ where positive values are outside the surface and negative values are inside the surface. In this way the morphologies are implicitly defined as the surface can be found through interpolation at the zero level set. Then using a set of surface points, contact is established when the location of a surface point from a leader particle returns a negative level set value from the follower particle (Fig. 1). Like in other DEM variants this necessitates a small overlap between particles to occur to determine contact with an assumption made that the overlap is too small to affect results.

The surface normal vector is then determined by taking the gradient of the level set function at that point,

$$\nabla\phi(\mathbf{x}) = \hat{\mathbf{n}} \tag{1}$$

Both the overlap and surface normal is used to get contact force through a force–displacement relationship based contact model. No contact model is specific to LS-DEM, however it is important to consider that contact force is heavily determined by the local curvatures of the contacting surfaces. Hertzian contact is often used in other DEM variants, however this model is only accurate for spheres [20]. Due to the high variety of possible contacting curvatures, a linear model will be used with the assumption that having enough contacts will average out the error. The linear model has been shown many times to give reasonable results for LS-DEM [16]. Both normal and pre-slip shear forces use the linear model,

$$\mathbf{F}_n = k_n \delta_n \hat{\mathbf{n}} \tag{2}$$

$$\Delta\mathbf{F}_s = k_s v_s \Delta t\, \hat{\mathbf{s}} \tag{3}$$

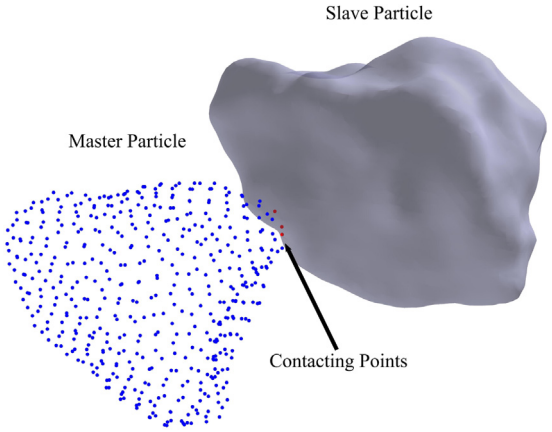

Fig. 1. Illustration of LS-DEM contact. Red surface points are inside the follower particle and are therefore considered in contact. (For interpretation of the references to color in this figure legend, the reader is referred to the web version of this article.)

where k_n and k_s are the normal and shear stiffnesses respectively, v_s is the relative velocity in the shear direction between contact points, and Δt is the timestep. Using Coulomb friction, the shear force has a maximum value which allows slip,

$$\mathbf{F}_s^{max} = \mu \| F_n \| \tag{4}$$

where μ is the static friction coefficient. Due to the frictional aspect being history dependent, shear forces use an incremental approach. Moment is calculated by crossing the total contact force with the vector pointing from the center of mass of the particle to the contact point, $\mathbf{c}$,

$$\mathbf{M} = \mathbf{c} \times \mathbf{F} \tag{5}$$

Once forces and moments are found, the kinematics are calculated using Newton's laws and a global damping formulation. Global damping, which is controlled by the global damping parameter, ξ, is applied as described in Lim et al. [21] for both translational motion,

$$v^{n+1/2} = \frac{1}{1 + \xi \Delta t/2} \left[(1 - \xi \Delta t/2) v^{n-1/2} + \frac{\Delta t}{m} F \right] \tag{6}$$

and also rotational motion, which uses an iterative predictor–corrector procedure to converge to the correct angular velocities. The algorithm is described in full in Lim et al. and is an integration of Euler's equations of motion with inertia proportional damping,

$$\alpha_1 = [M_1 + \omega_2 \omega_3 (I_2 - I_3) - \xi I_1 \omega_1]/I_1 \tag{7}$$

$$\alpha_2 = [M_2 + \omega_3 \omega_1 (I_3 - I_1) - \xi I_2 \omega_1]/I_2 \tag{8}$$

$$\alpha_3 = [M_3 + \omega_1 \omega_2 (I_1 - I_2) - \xi I_3 \omega_1]/I_3 \tag{9}$$

Global damping is not always added for DEM simulations but is often useful. The explicit time integration used in DEM often commands the use of small time steps and therefore higher rates of forcing to maintain reasonable simulation durations [22,23]. The global damping alleviates the dynamic errors introduced by maintaining quasi-static conditions.

2.2. Bonding model

Particle bonding models in DEM can usually be described within two different types which have been termed the parallel bonding model and the contact bonding model when introduced [6]. In LS-DEM-BPM both of these variants may be implemented as shown in Fig. 2.

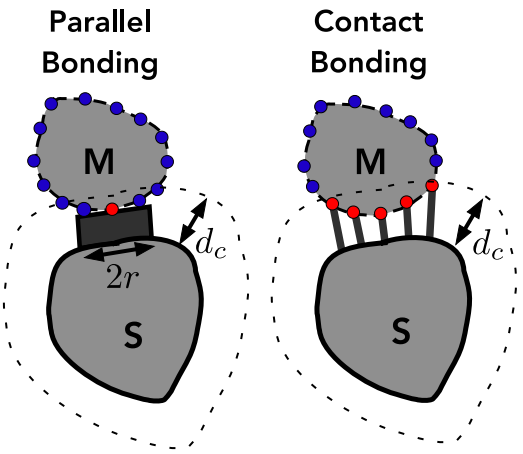

Fig. 2. Sketch in 2D of each bonding model for a single leader–follower bond pair. Note that for parallel bonding only the closest point is used to make a bond while for contact bonding all points closer than d_c are used.

The parallel bonding model connects contact points with a bond that resists relative motion and relative rotation. Bonding points are determined at the initialization step of the simulation by searching for nearby particles. In LS-DEM-BPM, this is done in a manner similar to contact where two particles are bonded if a surface point of a leader particle is within a maximum bonding distance of the surface of the follower particle. This is determined by evaluating the follower particle's level set function at the leader particle's surface point location. This maximum bonding distance is set by the user and is termed the cohesive distance, d_c. For the case of parallel bonding, only the surface point that returns the smallest level set value from the follower particle is used.

The contact bonding model is similar to the parallel bonding model except the bonds have infinitesimal thickness and therefore do not resist rotation. A clear use for this in LS-DEM-BPM is by allowing many contact bonds per particle pair that together can resist rotation while simultaneously allowing for the bond to not necessarily break all at once.

While in this paper the linear method will be used for both parallel and contact bonding, neither are limited by this. Non-local methods have shown to provide accurate results and can be implemented by modifying the model similarly to the studies where it was implemented with spheres [7,8].

2.2.1. Bonding mechanics

Each parallel bond is made with a defined radius, r, that defines the cross-section of a cylindrical beam that connects the bond points. Circular cross sections are used because they bear the closest resemblance in shape to a sinter neck, adhesive or any other bonding agent. This radius is used to compute the bond area, $\bar{A}$, and moment of inertiae for both the rolling, $\bar{I}$, and twisting, $\bar{J}$, axes of motion,

$$\bar{A} = \begin{cases} 2rt, & t = 1, 2D \\ \pi r^2, & 3D \end{cases} \quad \bar{I} = \begin{cases} \frac{2}{3} r^3 t, & t = 1, 2D \\ \frac{1}{4}\pi r^4, & 3D \end{cases} \quad \bar{J} = \left\{ \frac{1}{2}\pi r^4, \quad 3D \right. \tag{10}$$

The bar above variables in this section identify variables as pertaining to bonding characteristics, for example $\bar{I}$ is the moment of inertia for the bond and I is the moment of inertia for a particle. Bonds act on particles through a force displacement relationship and a moment angle relationship calculated incrementally in both the normal and shear directions.

$$\Delta \bar{F}_n = \bar{k}_n \bar{A}\, v^p_{rel,n} \Delta t \tag{11}$$

$$\Delta \bar{F}_s = \bar{k}_s \bar{A}\, v^p_{rel,s} \Delta t \tag{12}$$

$$\Delta \bar{M}_n = \bar{k}_s \bar{J} \omega_{rel,n} \Delta t \tag{13}$$

$$\Delta \bar{M}_s = \bar{k}_n \bar{I} \omega_{rel,s} \Delta t \tag{14}$$

where the total force and moment from the bond can be computed by adding the normal and shear components

$$\bar{\mathbf{F}} = \bar{F}_n \hat{\mathbf{n}} + \bar{F}_s \hat{\mathbf{s}} \tag{15}$$

$$\bar{\mathbf{M}} = \bar{M}_n \hat{\mathbf{n}} + \bar{M}_s \hat{\mathbf{s}} \tag{16}$$

The variables $\bar{k}_n$ and $\bar{k}_s$ are the stiffnesses in both the normal and shear directions for the bond. The normal stiffness can be understood by considering the elasticity of the adhesive agent. Suppose a bonding agent has a Young's modulus, $\bar{E}$, then the stiffness could be calculated from knowledge of the cylindrical geometry of the bond. Here the area we have just determined, and the length is approximately the cohesive distance used as our search area to determine bonding,

$$\bar{k}_n = \frac{\bar{E}\bar{A}}{d_c} \tag{17}$$

The shear stiffness can be similarly understood with the shear modulus, $\bar{G}$, or more often is set as a ratio between the shear stiffness and the normal stiffness.

The bonds are allowed to break, which is determined by stresses computed using the following beam equations,

$$\bar{\sigma}_c > \bar{\sigma} = \frac{\bar{F}_n}{\bar{A}} + \frac{|\bar{M}_s| r}{\bar{I}} \tag{18}$$

$$\bar{\tau}_c > \bar{\tau} = \frac{|\bar{F}_s|}{\bar{A}} + \frac{|\bar{M}_n| r}{\bar{J}} \tag{19}$$

Bond breakage occurs when the total stress in the beams exceed a breakage stress. When a bond breaks, the bond is eliminated from the model and therefore does not produce any further forces or moments.

For the case of using contact bonding, there is no concept of bond thickness or moment resistance which simplifies the bond force equations to,

$$\Delta \bar{F}_n = \bar{k}_n \, v^p_{rel,n} \Delta t \tag{20}$$

$$\Delta \bar{F}_s = \bar{k}_s \, v^p_{rel,s} \Delta t \tag{21}$$

Note that the bond stiffness is different here than in parallel bonding. The two definitions of bond stiffness can be related to each other in the following way,

$$\bar{k}_n^{contact} = \frac{\bar{k}_n^{parallel} \bar{A}}{\bar{n}} \tag{22}$$

where $\bar{n}$ is the number of contact bonds for the interface. The breakage condition is also simplified to being a critical breakage force rather than a breakage stress.

$$\bar{F}_{n,c} > \bar{F}_n \tag{23}$$

$$\bar{F}_{s,c} > \bar{F}_s \tag{24}$$

The critical breakage forces can still be determined by breakage stress however with knowledge of the discretization density of the surface points per unit surface area, ρ_p,

$$\bar{F}_{n,c} = \frac{\bar{n}\bar{\sigma}_c}{\rho_p} \tag{25}$$

$$\bar{F}_{s,c} = \frac{\bar{n}\bar{\tau}_c}{\rho_p} \tag{26}$$

2.2.2. Bond damping

Without damping in the model, the bond forces will oscillate which would cause premature breakages and instability. For many applications, particularly for quasi-static tests, global damping is enough to remove these oscillations. Applications with more dynamic interaction prefer to not use global damping however, which requires an ability to dampen bond motion locally. The goal of local bond damping is for both the translational and rotational motion of the bonded contact to be critically damped so that the stress in the bond is equilibrated at the fastest rate.

For translational motion the normal equation for critical damping in a one degree of freedom system is used,

$$\bar{F}^{damp} = v_n \left[2\sqrt{\bar{k}_n \bar{A} m^{eq}} \right] - v_s \left[2\sqrt{\bar{k}_s \bar{A} m^{eq}} \right] \tag{27}$$

where the first term controls the damping in the normal direction to the surface of the particles and the second controls damping in the shear direction. The term m_{eq} is the equivalent mass computed from the masses of each bonded particle,

$$m_{eq} = \frac{m^{(1)} m^{(2)}}{m^{(1)} + m^{(2)}} \tag{28}$$

Rotations are considered similarly,

$$\bar{M}^{damp} = \omega_n \left[2\sqrt{\bar{k}_s \bar{J} I_n^{eq}} \right] + \omega_s \left[2\sqrt{\bar{k}_n \bar{I} I_s^{eq}} \right] \tag{29}$$

where I_n^{eq} and I_s^{eq} are the normal and shear equivalent moments of inertia calculated from the normal and shear moments of inertia from each particle at the point of bonding. For example in the normal direction I_n^{eq} can be calculated as,

$$I_n^{eq} = \frac{I_n^{(1)} I_n^{(2)}}{I_n^{(1)} + I_n^{(2)}} \tag{30}$$

and the normal moment of inertia can be found from the parallel axis theorem being applied to the scalar moment of inertia about the normal axis which is determined from the particle's moment of inertia tensor,

$$I_n = (\hat{\mathbf{n}} \cdot \mathbf{I})\hat{\mathbf{n}} + m\|c\|^2 \tag{31}$$

In the case of contact damping, of course the damping moment is unused and the same equation for damping force can be used with just a simple change to the stiffness aspect,

$$\bar{F}^{damp} = v_n \left[2\sqrt{\bar{k}_n m^{eq}} \right] - v_s \left[2\sqrt{\bar{k}_s m^{eq}} \right] \tag{32}$$

In general it is recommended that either global damping or bond damping is used since applying both can easily over damp the system and therefore get inaccurate results from bond forces being unable to reach equilibrium. In cases of low global damping though, the bond damping force can still be applied but may need to be scaled down for achieving the best results.

By combining this section with the previous two, the mathematics for calculating forces and moments can be understood. To illustrate how all the mechanics come together in implementation, a pseudocode is shown below for calculating contact and bonding for a single particle pair.

Algorithm 1 Calculate forces and moments

```
for all particle pairs {i, j} ← {leader, follower} do
  for all surface points of leader particle, p_i do
    if surface point and follower particle have intact bond then
      {Get Bond Forces and Moments} F̄_n, F̄_s, M̄_n, M̄_s ← Eqs. (11), (12), (13), (14)
      {Check for Breakage} σ̄, τ̄ ← Eqs. (18), (19)
      if Eqs. (18) & (19) false then
        Set bond to broken
      else
        {Apply Damping} F̄^damp, M̄^damp ← Eqs. (27), (29)
      end if
    else if φ_j(p_i) < 0 then
      {Get Contact Surface} n̂, ŝ ← Eqs. (1), v_s/||v_s||
      {Get Forces and Moments} F_n, F_s, M ← Eqs. (2), (3), (4), (5)
    end if
  end for
end for
```

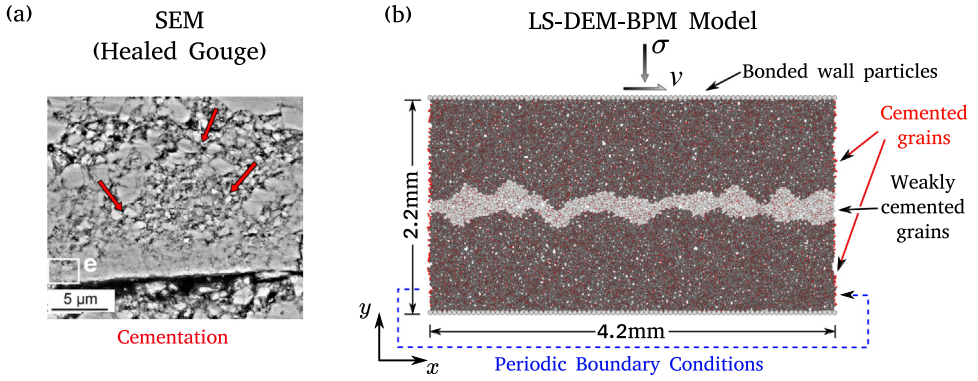

Fig. 3. (a) SEM micrograph of a healed gouge adopted from [34]. Arrows show cohesive bridges (bonds) forming between aggregates (b) Idealized numerical model of the fault.

3. Model behavior for fault rupture tests

In this first application of the proposed methodology, we model the rupture of a fault subjected to compression and shear, and the ensuing formation of a granular gouge. In particular, we focus on modeling the fracture of surface asperities and the deterioration of cementation at the grain scale, and we identify their effect on the macroscopic friction. A plethora of experimental studies have focused on delineating this macroscopic frictional behavior for a natural or model fault [24–26], which have inspired a series of theories [27,28] culminating in the development of the rate-and-state framework [29,30]. However, these theories remain largely phenomenological given the relative sparsity of micromechanical modeling of these complex grain-scale processes. DEM enhanced with contact aging was employed in [31] to investigate the frictional behavior of gouge, and reproduce several characteristics observed in the laboratory. Further, DEM with bonding was used in [32] to study gouge formation under constant-velocity shearing of two surfaces, and in [33], to study the effect of the heterogeneity of the slip surface on the overall characteristics of the slip behavior. In the following, we will present how LS-DEM-BPM can be used to gain further insight into the frictional response of a fault, and we will discuss its implications to rate-and-state theory.

3.1. Setup

Fig. 3a shows an SEM micrograph of a natural gouge, which has been subjected to chemical healing processes, inducing cementation between aggregates [34,35]. Fig. 3b shows the idealization of that system within the proposed framework. In particular, we consider a 2D cell comprised of 10,000 angular particles modeled after a quartz sand [36] bonded together. The process of cementation is modeled by parallel bonding neighboring particle surface points that lie within a threshold distance as described in Section 2.2. The properties of particles and cement bonds are reported in Fig. 4. We will further assume that the grains themselves cannot experience fracture, although such an extension is possible within the LS-DEM framework [37].

The cell is first vertically compressed to a pressure σ, allowing for periodic boundary conditions in the x-direction. To impose shear, the upper wall is displaced horizontally, while keeping a constant vertical stress. A preimposed weak interface is introduced in the middle of the specimen, in order to control the initiation of the rupture (Fig. 3b). The velocity of the upper wall is first kept constant at a value $v_0 = 1\,\text{mm/s}$ until steady state is achieved, and is then instantaneously increased to a value $v_f = 10\,\text{mm/s}$, until the new steady state is reached (Fig. 5a). During this process, we measure the evolving population of interparticle bonds as well as the shear stress at the upper boundary, yielding the transient macroscopic friction angle $\mu = \tau/\sigma$.

3.2. Rate-and-state friction law

Before delving into the results of the numerical experiments, we briefly review the standard rate-and-state friction law used to describe these systems. The law relies on the Coulomb assumption with a rate and state dependent

Parameter	Value	Units
Density (ρ)	2500	Kg/m^3
Grain Young's modulus (E_g)	70	GPa
Contact stiffness ratio (k_n/k_t)	2	-
Friction coefficient (μ)	0.3	-
Coefficient of restitution (c_r)	0.6	-
Cement Young's modulus ($\bar{E}_c$)	3	GPa
Bond stiffness ratio ($\bar{k}_n/\bar{k}_t$)	2	-
Cement compressive strength ($\bar{\sigma}_c$)	100	MPa
Cement shear modulus ($\bar{\tau}_c$)	100	MPa

Fig. 4. Particle and cement properties for the LS-DEM-BPM model of the gouge.

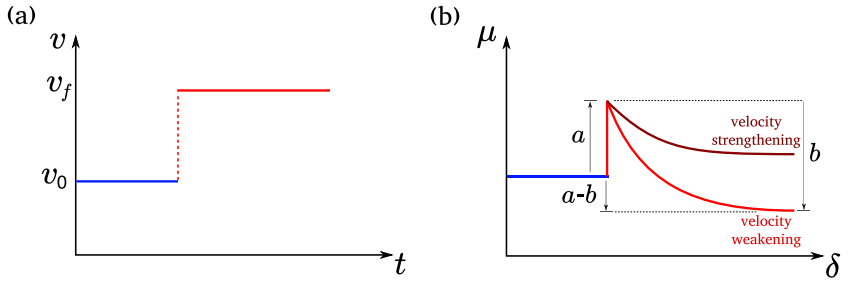

Fig. 5. (a) Velocity history (b) Rate-and-state friction law.

friction coefficient $\tau = \mu(v, \theta)\sigma$, where v is the slip rate and θ is an internal variable (state) representing history dependence, typically interpreted as the contact lifetime:

$$\mu = \mu_0 + a \log \frac{v}{v_0} + b \log \frac{v_0 \theta}{L} \tag{33}$$

where μ_0, v_0 are the reference friction coefficient and reference velocity, respectively, L is a length scale, and a, b are parameters of the model. The evolution of state is described by the aging law [29]:

$$\dot{\theta} = 1 - \frac{v\theta}{L} \tag{34}$$

and can give rise to either velocity strengthening ($a - b > 0$) or velocity weakening ($a - b < 0$). Fig. 5 demonstrates the evolution of friction in these two cases. For bare slipping surfaces, experimental evidence suggest velocity weakening behavior [25]. In the presence of gouge, most evidence points to velocity strengthening [25], while velocity weakening has also been reported in the literature [38,39], depending on the inertial number [40,41].

3.3. Results

Fig. 6a shows the evolution of macroscopic friction against the fault slip for the same experiment carried out at two different pressures $\sigma_1 = 1$ MPa and $\sigma_2 = 2$ MPa respectively. Following the initial rupture at the weak interface, both systems arrive at a steady state as witnessed by the small fluctuations in friction. These fluctuations represent stick–slip events arising from the repeating formation and collapse of force chains. This is evident in Fig. 7a, which shows the heterogeneous contact force and bond force chains at that state for the higher pressure experiment. Fig. 6b shows the rate of bond breaking for the two experiments. After an initially pronounced bond breaking phase, we observe a decrease in the rate of bond breaking towards the first steady state, at a slip of approximately 2 mm.

Upon the imposed sudden increase in the velocity in the second stage of the experiments, we observe a spontaneous increase in friction in line with experimental evidence and rate-and-state theory. This so-called "direct effect" is the signature of an increase in the number of activated contacts. Gradually, the contact network rearranges

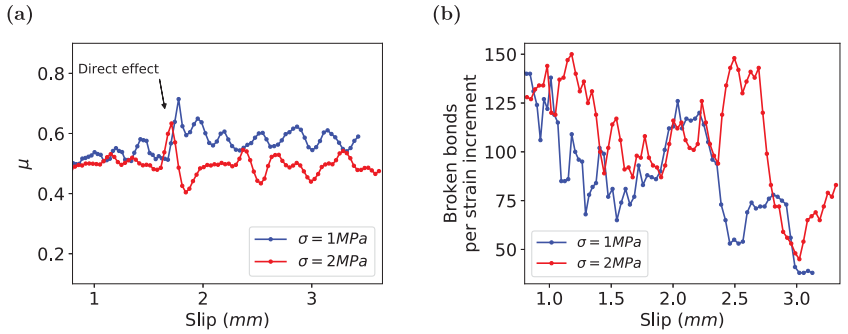

Fig. 6. (a) Friction as a function of slip (b) Rate of bond breakage (averaged over 1% shear strain increments) as a function of slip.

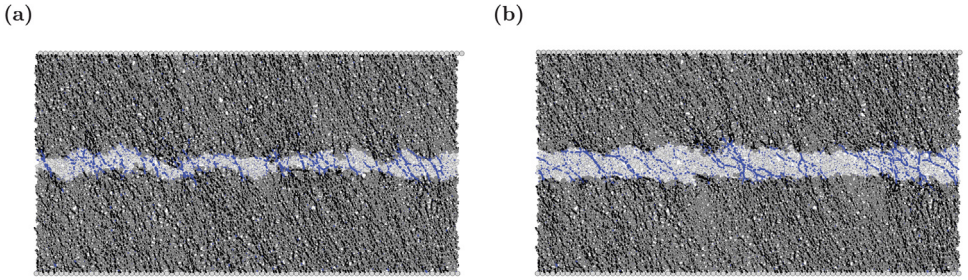

Fig. 7. Particle configuration with bond force chains (in black) and contact force chains (in blue) for the low pressure experiment for states (a) right before the velocity jump and (b) at the final steady state. Darker particles represent those connected by cement bonds; Lighter particles represented unbonded particles. (For interpretation of the references to color in this figure legend, the reader is referred to the web version of this article.)

itself, and force chains appear to localize at the asperities (Fig. 7a). We observe local fractures at the asperities as a result of these dynamic stress concentrations. This leads to widening of the gouge, and in turn to reduced particle interlocking which reduces macroscopic friction. In Fig. 6b, we observe that the rate of bond breaking indeed increases in both systems at a slip >2 mm, only to eventually decay towards a new steady state at a slip > 3 mm. At that point only few bonds continue to experience fracture. The widened fault at the final steady state is shown in Fig. 7b for the lower pressure experiment. The final steady state friction coefficient depends on the pressure, which affects the accumulated damage to the asperities and alters the dynamics of the contacting particles within the weakened zone. In this experiment we observe that lower pressure leads to rate-strengthening behavior, while a higher pressure leads to minor rate-weakening behavior which is likely due to greater damage at the asperities.

Although no direct comparison with experiments is attempted in this study, this framework exhibits great potential in reproducing the range of behaviors observed in the laboratory. The incorporation of particle morphology ensures that we can accurately account for particle interlocking and rolling, which has been shown to be important for fault gouge modeling [42]. This completely avoids the need for numerical proxies, when approximating the system by idealized shapes such as disks [31]. Further, the incorporation of local (particle surface) bonding ensures an accurate representation of contact scale cementation. Uncovering the complex interplay between the inertial properties of the gouge, and the evolving surface roughness and gouge width [43], would clearly require a systematic investigation of the parameters of the system. The latter could then shed light on the parameters of the rate-and-state theory, such as the length scale L. The above lie beyond the scope of this application.

4. Model behavior for cone penetration tests

This application will study the model behavior during a cone penetration test. Particularly we will look at the effect of sintering neck size on strength. The sintering process is an important aspect for many classes of materials such as metals and ices. Being able to predict the changes in strength with increasing amounts of sintering is highly desirable.

Parameter	Value	Units
Density (ρ)	900	$\mathrm{Kg/m^3}$
Grain Young's modulus (E_g)	9	GPa
Contact stiffness ratio (k_n/k_t)	2	-
Friction coefficient (μ)	0.2	-
Coefficient of restitution (c_r)	0.6	-
Cement Young's modulus ($\bar{E}_c$)	9	GPa
Bond stiffness ratio ($\bar{k}_n/\bar{k}_t$)	2	-
Cement compressive strength ($\bar{\sigma}_c$)	1	MPa
Cement shear modulus ($\bar{\tau}_c$)	1	MPa

Fig. 8. Particle and cement properties for the LS-DEM-BPM model of the ice specimen.

An example of an application where understanding the strength of a sinter network in a granular material is sample acquisition on space missions to icy worlds. NASA has made it a priority to send missions to moons in the solar system with global oceans such as Europa and Enceladus due to the relatively high probability of finding life [44]. Due to the very low temperatures and near vacuum conditions, porous ice solidifies at a very slow rate meaning the planetary surface likely remains quite porous [45]. Due to this, large amounts of the surface would correctly be described as a connected granular material. This is particularly true for the most geologically active areas, which are often of highest interest, such as the south pole region of Enceladus. This region has geysers emitting ice particles from the subsurface that either eject into Saturn's E-ring or fall back onto the nearby surface [46]. This section is built to be a first attempt at mimicking a metal cone penetrating an icy surface such as Enceladus in this region where ice is granular.

4.1. Specimen preparation

The specimen was prepared by pluviation of particles into a cylindrical container. A set of 100 unique granular geometries were used as particles taken from an XRCT image of Hostun sand. During pluviation, the particles were made slightly larger so that when the specimen is complete there is empty space where the sintered necks will be. Instead of all the particles being dropped from the beginning, particles were only added when previous particles had settled. Each new set of added particles were placed directly above the specimen, resulting in the particles depositing at a low velocity. This created a loose specimen with a porosity of 46%. Particle parameters used during the pluviation process were the same as during testing and are shown in Fig. 8. When bonding the particles, a cohesive distance of 0.5 mm was used with several neck sizes.

4.2. Cone penetration test

The cone penetration test was conducted by descending a cone with a diameter of 1 cm at a rate of 0.2 m/s into the ice specimen. Considerable global damping was used to ensure quasi-static conditions despite the relatively high penetration rate. Due to this, no bond damping was necessary for this case. The stress was calculated by adding up the vertical forces on the cone tip and dividing by the cross sectional area of the cone. The test is conducted three times to investigate the effect of the thickness of the sintered neck being represented as bonds. The thickness is set by a ratio between the radius of the sintered neck, r, and the radius of the circumscribed sphere of each particle, R. The three thicknesses tested are $r/R = 0.01$, $r/R = 0.25$ and $r/R = 0.5$. Fig. 9 shows a visualization of the cone penetrating the ice specimen at various stages of loading for $r/R = 0.5$. During the early stages of the loading, such as in Figs. 9c and 9d where the cone displacement is at 1.5 cm, small cracks near the tip can easily be observed with these cracks causing only local deformation in the area of the cracking. In Fig. 9d it can be observed that cracking propagates laterally as the particles are pushed away from the cone center, however the bonds remain intact directly below the tip providing continued resistance. At this time of loading stress is continuing to build with occasional minor cracks causing only minimal reductions in strength as seen in Fig. 10. Above a displacement of a little over 2 cm the specimen experiences heavy brittle fracture for both $r/R = 0.25$ and $r/R = 0.5$. In the

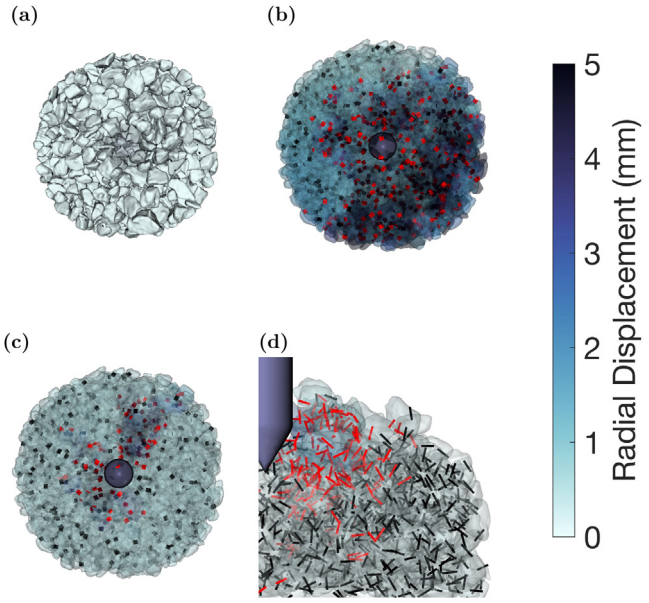

Fig. 9. Visualization of ice specimen with $r/R = 0.5$. Color indicates the displacement of the particle away from the center of the specimen with darkest color being a displacement of one cone radius. Black lines indicate intact bonds and red lines are broken bonds. (a) Top view of initial specimen. (b) Specimen after complete fracture. (c) Top view at 1.5 cm cone displacement. (d) Profile of specimen at 1.5 cm cone displacement. (For interpretation of the references to color in this figure legend, the reader is referred to the web version of this article.)

visualization in Fig. 9b, large displacements and heavy breakage can be easily observed in most of the specimen corresponding to the large stress drop measured.

For the test where $r/R = 0.01$, the very low sintering results in very little resistance which is expected. For this case the specimen does not experience the same reductions in strength from heavy breakage but instead has a much more consistent level of resistance as what may be expected from a specimen with no bonding at all.

This model behavior is consistent with trends seen for ice that experiences brittle breakage with the advantage of being able to investigate the micromechanics of the sintered bonds [47]. In future work with modeling strength of sintered particles it would be advantageous to utilize the shape morphing aspects of the level set method to better represent particles morphologies and different stages of sintering. Level sets are extensively used for tracking shape changes from physical processes [19]. Implementing the many theoretical models that predict sinter growth with the level set evolution methods is a promising avenue for more accurate modeling in the future.

The results for the cone penetration test show the considerable affect the thickness of particle bonds have on the behavior of the model, and therefore the importance of understanding how particles adhere together. A common assumption in BPM is to take the thickness of the bond as the minimum of the thicknesses of the two particles being bonded. This likely a good assumption for non-porous material such as rock where the cementation completely surrounds each particle, but probably an insufficient assumption for more porous substances such as ice or metal that has not been fully sintered together.

5. Model behavior for adhesive failure

There are many instances where an adhesive agent that is wished to be modeled between particles may not break all at once. In these cases, modeling with a single breakable bond is not ideal since relative rolling between particles should cause failure in only the tensile region of the bond. In order to model these cases, this section proposes to have multiple contact bonds at each contact pair instead of a single parallel bond. Here an example of this idea is presented with a simple constructed material built to absorb energy. The construction of periodic and lattice structures to tune viscoelastic behavior is common in applications from the nanoscale [48] to the macroscale [49]. In this study, the choice of structure is a lattice of very stiff spheres bonded with a compliant adhesive. While LS-DEM-BPM could handle any other geometry just as well, spheres show that for this case the utilization of

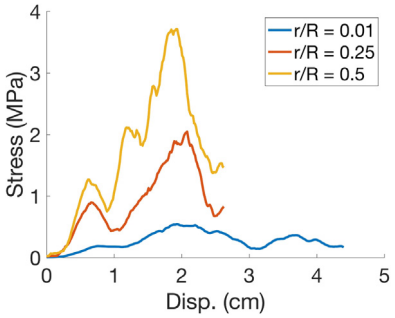

Fig. 10. Relationship between stress on cone and cone displacement into the specimen for various sinter neck thicknesses. Due to the brittle nature, the cone stress on specimens with thicker bonds falls abruptly at a critical level.

Parameter	Value	Units
Density (ρ)	2650	Kg/m^3
Grain Young's modulus (E^*)	66	GPa
Contact stiffness ratio (k_n/k_t)	2	-
Friction coefficient (μ)	0.1	-
Coefficient of restitution (c_r)	0.6	-
Cement Young's modulus ($\bar{E}_c$)	0.2	MPa
Bond stiffness ratio ($\bar{k}_n/\bar{k}_t$)	2	-
Cement compressive strength ($\bar{\sigma}_c$)	11	MPa
Cement shear modulus ($\bar{\tau}_c$)	11	MPa

Fig. 11. Particle and cement properties for the LS-DEM-BPM model of the sphere specimen.

surface points for bonding delivers the advantage of having multiple bonds per particle pair that may be useful enough even for sphere based applications.

5.1. Model setup

A cubical lattice specimen was prepared by placing spheres in a five by five grid. Each sphere was allowed to bond only vertically, allowing spheres to move laterally. This was done so that the structure could buckle more easily therefore increasing its potential for dissipation. Spheres were ordered so that leader particles were placed below follower particles, so therefore bonds are centered at the surface of the bottom particles and directed toward the top particle. The surface points for each sphere were seeded so that each bond is made of 14 separate and evenly spaced contact bonds. Walls were added to the top and bottom of the specimen with equal stiffness and friction to the spheres. The specimen is shown in Fig. 12a in the initial state before compression. Whereas normally in LS-DEM a linear contact model is used, for this case a Hertzian contact model is used due to the spherical shapes, changing the force displacement relationship to,

$$F_n = \frac{4}{3} E^* \sqrt{R\delta_n^3} \tag{35}$$

where R is the effective radius which for uniform spherical contact is equal to half the sphere radius and for sphere to wall contact is the equivalent to the sphere radius. The material parameter E^* is defined in the usual way for contact of identical materials,

$$E^* = \frac{E}{2(1-\nu^2)} \tag{36}$$

Exact model parameters used are shown in Fig. 11. The value of breakage stress for the bonds in this example was normal distributed across the interfaces which will provide some heterogeneity to the otherwise identical sphere columns.

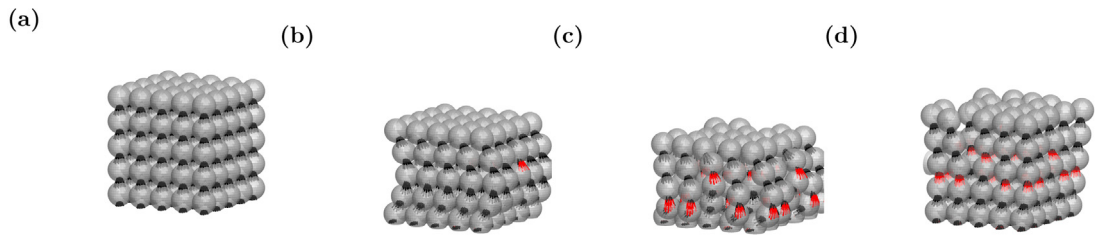

Fig. 12. Visualization of the compression of spheres bonded with the contact bonding model. (a) Initial state (b) 10% strain (c) 20% strain (d) Fully unloaded.

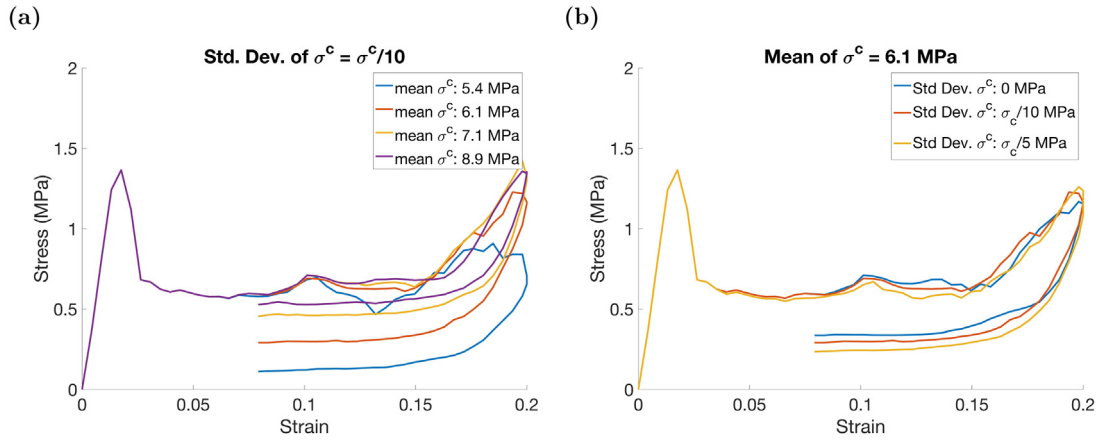

Fig. 13. The stress vs. strain relationship for various levels of bond strength. Figure (a) shows plot for various mean values for critical stress. Figure (b) shows plot for various standard deviations of critical stress.

5.2. Model results

The specimen underwent one full loading and unloading cycle with a peak strain of 20% for each test conducted. Stresses were calculated by dividing the total force on the top wall by the maximum cross sectional area of the structure defined as, $A_{struc} = 10R_{sph}$ where R_{sph} is the radius of the spheres. Visualizations of the simulations were rendered to observe bulk behavior in the specimen shown in Fig. 12. It can first be observed that breakages generally occur in the middle row of bonds, which is sensible since that is the area where the highest stress will naturally occur. Bond breakage does however occur outside of the middle row as well to a lesser degree. After unloading, most columns appear to come back to full height, showing evidence that very high levels of deformation do not injure the ability of the bonding method to recover the initial state.

Constitutive behavior of the specimen can be seen in Fig. 13. During loading, three distinct phases of behavior can easily seen for all cases tested. First is the pre-buckling phase where the structure behaves closely to the material behavior of the spheres. The structure then buckles, resulting in nearly constant stress with limited evidence of bond breakages. Finally, considerable bond breakages occur while simultaneously the densification of the spheres create new sphere to sphere contacts resulting in higher strength.

Upon unloading, significant hysteresis is observed the magnitude of which being inversely proportional to the average bond strength as shown in Fig. 13. Interestingly, the variance of the bond strength has a minor effect as well, where a higher variance in bond strength causes more hysteresis. This can be explained by the fact that higher variance of bond strengths results in more bonds being broken if stresses in the bonds on average remain lower than the average critical stress.

6. Discussion

The most considerable advantage to using LS-DEM-BPM is the ability to use any arbitrary shape. For a fully bonded granular material, particle shape will affect the fabric of the bonds as it does the fabric of contact forces

for an un-bonded granular material. For cases where there are very few fully debonded particles, the polyhedron method could be sufficient since the interlocking effect of concave features may not play as large of a role as it would for an un-bonded granular material. However, an interesting direction of future work with using level sets will be utilizing images of the microscale for materials such as rock or sintered materials to investigate the importance of grain shape in the material behavior. XRCT and SEM images of the grain-scale for these materials allow access to the true shape characteristics of the grains and grain boundaries. With plenty of research confirming that fractures generally occur along grain boundaries, representing the correct shape for the grains will likely prove to be a key aspect for using BPM for such applications [50].

The advantage of arbitrary shape becomes even more pronounced in applications such as the fault gouge where the material behavior beyond the breakage of bonds is important. Once particles have broken all of their bonds, those particles will behave as an un-bonded granular material. The importance of particle shape in an un-bonded granular material is well documented [51] and has been the driving reason for many DEM variants attempting to define shape in general ways [52]. Especially for the fault gouge where shear is the driving mechanism for deformation, the correct particle shape is critical as it has the largest effects on the predictions for shear [53].

The most significant disadvantage with LS-DEM-BPM continues to be the efficiency of the method. Some applications ask for the simulation of millions of particles, and while this is certainly possible with LS-DEM-BPM it is unfeasible without large computational resources. New developments in efficiency with LS-DEM such as using octree methods may prove to alleviate though not completely solve this issue [54]. Until the new generations of computer processors or the implementation of LS-DEM with GPU parallelization, LS-DEM is limited to particle numbers on the order of $< 10^6$ particles. This limitation is important for applications where a granular specimen must interact with large objects, however studies for even these cases will often show that there are diminishing returns for using smaller and smaller particles [55]. For cases where the goal of the modeling is to investigate the material behavior by using a representative volume element, this limitation is less important as many studies have shown success at replicating experiment with much fewer particles [56].

7. Conclusion

The implementation of the bonded particle method with the level set discrete element method has been introduced. This allows the bonded particle method to be utilized with a DEM method that allows for arbitrary particle shape. Examples of possible applications of this method have been shown. The fault gouge example demonstrated the capability of the method to model a fault gauge and the rate-state friction model. This example highlighted the potential for this model in applications where the unbonded granular materials play a significant role. An example of a cone penetrometer fracturing ice demonstrated the effects of bond thickness on the model behavior is significant. The third example showed the potential for a modeling strategy where each particle pair may have many bonds that do not necessarily break all at once. This strategy allows for crack growth within each particle bond and correctly weakens only the bonding region where tensile forces were present. Finally a discussion highlighted the advantages of particle shape despite drawbacks in efficiency. This procedure could open doors to new knowledge of materials that can be defined as a connected granular material.

Declaration of competing interest

The authors declare that they have no known competing financial interests or personal relationships that could have appeared to influence the work reported in this paper.

Acknowledgment

This work was supported by a NASA Space Technology Research Fellowship, United States of America, Grant No. 80NSSC19K1160.

References

[1] D.E. Grady, M.E. Kipp, The micromechanics of impact fracture of rock, Int. J. Rock Mech. Min. Sci. Geomech. Abstr. 16 (5) (1979) 293–302.

[2] J.B. Regnet, Christian David, Philippe Robion, Beatriz Menéndez, Microstructures and physical properties in carbonate rocks: A comprehensive review, Mar. Pet. Geol. 103 (03) (2019).

[3] W. Weibull, A Statistical Theory of the Strength of Materials, Handlingar/Ingeniörsvetenskapsakademien. Generalstabens litografiska anstalts förlag, 1939.
[4] P.V. Hobbs, B.J. Mason, The sintering and adhesion of ice, Philos. Mag. J. Theor. Exp. Appl. Phys. 9 (98) (1964) 181–197.
[5] J. Christmann, R. Müller, K.G. Webber, D. Isaia, F.H. Schader, S. Kipfstuhl, J. Freitag, A. Humbert, Measurement of the fracture toughness of polycrystalline bubbly ice from an antarctic ice core, Earth Syst. Sci. Data 7 (1) (2015) 87–92.
[6] D.O. Potyondy, P.A. Cundall, A bonded-particle model for rock, Int. J. Rock Mech. Min. Sci. 41 (8) (2004) 1329–1364, Rock Mechanics Results from the Underground Research Laboratory, Canada.
[7] Miguel Celigueta, Salvador Latorre, Ferran Arrufat, Eugenio Oñate, Accurate modelling of the elastic behavior of a continuum with the discrete element method, Comput. Mech. (2017).
[8] F. Arrufat, M.A. Celigueta, S. Latorre, E. Oñate, An accurate nonlocal bonded discrete element method for nonlinear analysis of solids: application to concrete fracture tests, Comput. Part. Mech. 7 (2020) 543–553.
[9] Xiao-Ping Steven Zhang, Louis Ngai Yuen Wong, Cracking processes in rock-like material containing a single flaw under uniaxial compression: A numerical study based on parallel bonded-particle model approach, Rock Mech. Rock Eng. 45 (2011) 711–737.
[10] Y.P. Cheng, Y. Nakata, M.D. Bolton, Discrete element simulation of crushable soil, Gé 53 (7) (2003) 633–641.
[11] M.B. Cil, K.A. Alshibli, 3d assessment of fracture of sand particles using discrete element method, Géotech. Lett. 2 (3) (2012) 161–166.
[12] Reid Kawamoto, Edward Ando, Gioacchino Viggiani, Jose E. Andrade, Andrade all you need is shape: Predicting shear banding in sand with ls-dem, J. Mech. Phys. Solids 111 (2018) 375–392.
[13] Wadi H. Imseeh, Khalid A. Alshibli, 3d finite element modelling of force transmission and particle fracture of sand, Comput. Geotech. 94 (2018) 184–195.
[14] S.A. Galindo-Torres, D.M. Pedroso, D.J. Williams, L. Li, Breaking processes in three-dimensional bonded granular materials with general shapes, Comput. Phys. Comm. 183 (2) (2012) 266–277.
[15] José V. Lemos, Discrete element modeling of masonry structures, Int. J. Archit. Herit. 1 (2) (2007) 190–213.
[16] Reid Kawamoto, Edward Andò, Gioacchino Viggiani, José E. Andrade, Andrade level set discrete element method for three-dimensional computations with triaxial case study, J. Mech. Phys. Solids 91 (2016) 1–13.
[17] Ivan Vlahinić, Edward Andò, Gioacchino Viggiani, José E. Andrade, Andrade towards a more accurate characterization of granular media: extracting quantitative descriptors from tomographic images, Granul. Matter 16 (1) (2014) 9–21.
[18] Liuchi Li, Eloise Marteau, José Andrade, Andrade capturing the inter-particle force distribution in granular material using ls-dem, Granul. Matter 21 (08) (2019).
[19] J.A. Sethian, Level Set Methods and Fast Marching Methods: Evolving Interfaces in Computational Geometry, Fluid Mechanics, Computer Vision, and Materials Science, in: Cambridge Monographs on Applied and Computational Mathematics, Cambridge University Press, 1999.
[20] K.L. Johnson, Contact Mechanics, Cambridge University Press, 1985.
[21] Keng-Wit Lim, José E. Andrade, Granular element method for three-dimensional discrete element calculations, Int. J. Numer. Anal. Methods Geomech. 38 (2) (2014) 167–188.
[22] O.R. Walton, R.L. Braun, Simulation of rotary-drum and repose tests for frictional spheres and rigid sphere clusters, 1993.
[23] Keng-Wit Lim, José E. Andrade, Granular element method for three-dimensional discrete element calculations, Int. J. Numer. Anal. Methods Geomech. 38 (2) (2014) 167–188.
[24] Carolyn A. Morrow, James D. Byerlee, Experimental studies of compaction and dilatancy during frictional sliding on faults containing gouge, J. Struct. Geol. 11 (7) (1989) 815–825, Friction phenomena in rock.
[25] Chris Marone, C. Barry Raleigh, C.H. Scholz, Frictional behavior and constitutive modeling of simulated fault gouge, J. of Geophys. Res. Solid Earth 95 (1990) 7007–7025.
[26] V. Rosakis A.J. Rubino, N. Lapusta, Understanding dynamic friction through spontaneously evolving laboratory earthquakes, Nature Commun. 8 (1) (2017).
[27] Christopher Scholz, Peter Molnar, Tracy Johnson, Detailed studies of frictional sliding of granite and implications for the earthquake mechanism, J. Geophys. Res. (1896-1977) 77 (32) (1972) 6392–6406.
[28] Yoshiaki Ida, Cohesive force across the tip of a longitudinal-shear crack and griffith's specific surface energy, J. Geophys. Res. (1896-1977) 77 (20) (1972) 3796–3805.
[29] James H. Dieterich, Modeling of rock friction: 1. experimental results and constitutive equations, J. Geophys. Res. Solid Earth 84 (B5) (1979) 2161–2168.
[30] Andy Ruina, Slip instability and state variable friction laws, J. Geophys. Res. Solid Earth 88 (B12) (1983) 10359–10370.
[31] Julia K. Morgan, Particle dynamics simulations of rate- and state-dependent frictional sliding of granular fault gouge, Pure Appl. Geophys. 161 (9) (2004) 1877–1891.
[32] Yonggui Guo, Julia K. Morgan, Fault gouge evolution and its dependence on normal stress and rock strength: Results of discrete element simulations: Gouge zone micromechanics, J. Geophys. Res. Solid Earth 113 (B8) (2008).
[33] Thomas Fournier, Julia Morgan, Insights to slip behavior on rough faults using discrete element modeling, Geophys. Res. Lett. 39 (12) (2012).
[34] S.A.F. Smith, S. Nielsen, G. Di Toro, Strain localization and the onset of dynamic weakening in calcite fault gouge, Earth Planet. Sci. Lett. 413 (2015) 25–36.
[35] Nynke Keulen, Holger Stünitz, Renée Heilbronner, Healing microstructures of experimental and natural fault gouge, J. Geophys. Res. Solid Earth 113 (B6) (2008).
[36] Konstantinos Karapiperis, Jason P. Marshall, José E. Andrade, Reduced gravity effects on the strength of granular matter: Dem simulations versus experiments, J. Geotech. Geoenviron. Eng. 146 (5) (2020) 06020005.

[37] John M. Harmon, Daniel Arthur, José E. Andrade, Level set splitting in dem for modeling breakage mechanics, Comput. Methods Appl. Mech. Engrg. 365 (2020) 112961.
[38] N.M. Beeler, T.E. Tullis, M.L. Blanpied, J.D. Weeks, Frictional behavior of large displacement experimental faults, J. Geophys. Res. Solid Earth 101 (B4) (1996) 8697–8715.
[39] Matt J. Ikari, Achim J. Kopf, Seismic potential of weak, near-surface faults revealed at plate tectonic slip rates, Sci. Adv. 3 (11) (2017).
[40] Osamu Kuwano, Ryosuke Ando, Takahiro Hatano, Crossover from negative to positive shear rate dependence in granular friction, Geophys. Res. Lett. 40 (7) (2013) 1295–1299.
[41] E. DeGiuli, M. Wyart, Friction law and hysteresis in granular materials, Proc. Natl. Acad. Sci. (2017).
[42] Julia K. Morgan, Numerical simulations of granular shear zones using the distinct element method: 2. effects of particle size distribution and interparticle friction on mechanical behavior, J. Geophys. Res. Solid Earth 104 (B2) (1999) 2721–2732.
[43] Christopher H. Scholz, Wear and gouge formation in brittle faulting, Geology 15 (6) (1987) 493–495.
[44] Christopher P. McKay, Ariel Anbar, Carolyn Porco, Peter Tsou, Follow the plume: The habitability of enceladus, 2014.
[45] J.L. Molaro, M. Choukroun, C.B. Phillips, E.S. Phelps, R. Hodyss, K.L. Mitchell, J.M. Lora, G. Meirion Griffith, The microstructural evolution of water ice in the solar system through sintering, J. Geophys. Res. Planets 124 (2) (2019) 243–277.
[46] Peter Tsou, Donald E. Brownlee, Christopher P. McKay, Anbar Ariel, Hajime Yano, Kathrin Altwegg, Luther W. Beegle, Richard Dissly, Nathan J. Strange, Isik Kanik, Life: Life investigation for enceladus a sample return mission concept in search for evidence of life, 2012.
[47] Erland M. Schulson, The structure and mechanical behavior of ice, JOM 51 (1999) 21–27.
[48] Carlos M. Portela, A. Vidyasagar, Sebastian Krödel, Tamara Weissenbach, Daryl W. Yee, Julia R. Greer, Dennis M. Kochmann, Extreme mechanical resilience of self-assembled nanolabyrinthine materials, Proc. Natl. Acad. Sci. 117 (11) (2020) 5686–5693.
[49] I. Maskery, N.T. Aboulkhair, A.O. Aremu, C.J. Tuck, I.A. Ashcroft, Compressive failure modes and energy absorption in additively manufactured double gyroid lattices, Addit. Manuf. 16 (2017) 24–29.
[50] Erik Eberhardt, B. Stimpson, Doug Stead, Effects of grain size on the initiation and propagation thresholds of stress-induced brittle fracture, Rock Mech. Rock Eng. 32 (1999) 81–99.
[51] Yu Guo, Jennifer Sinclair Curtis, Discrete element method simulations for complex granular flows, Annu. Rev. Fluid Mech. 47 (1) (2015) 21–46.
[52] Guilhem Mollon, Jidong Zhao, 3d generation of realistic granular samples based on random fields theory and fourier shape descriptors, Comput. Methods Appl. Mech. Engrg. 279 (2014) 46–65.
[53] John A. Herbst, Alexander V. Potapov, Making a discrete grain breakage model practical for comminution equipment performance simulation, Powder Technol. 143–144 (2004) 144–150.
[54] J. Duriez, C. Galusinsky, Level set representation on octree for granular material with arbitrary grain shape, 2020, pp. 64–71.
[55] Damiana Catanoso, Arno Rogg, Jennifer Case, Thomas Stucky, Analysis of sample acquisition dynamics using discrete element method, 2020.
[56] F. Froiio, J.-N. Roux, Incremental response of a model granular material by stress probing with dem simulations, AIP Conf. Proc. 1227 (1) (2010) 183–197.